THE JOURNAL OF PHYSICAL CHEMISTRY C

Article

Cite This: J. Phys. Chem. C 2019, 123, 17002−17009

pubs.acs.org/JPCC

Role of Superexchange Interactions on the Arrangement of Fe and Mn in $LiMn_xFe_{1-x}PO_4$

Yimeng Liu, Yue Gu, Hua Zeng, Jiaxin Zheng,* and Feng Pan*

School of Advanced Materials, Peking University, Shenzhen Graduate School, Shenzhen 518055, People's Republic of China

Supporting Information

ABSTRACT: Due to excellent safety and charge−discharge performances of $LiFePO_4$ (LFP), it has been widely studied as an important cathode material for lithium-ion batteries. The introduction of Mn ions to LFP materials to increase the voltage and energy storage is a hot topic that has attracted widespread attention. Our study focused on calculating the transition metal (TM) ion arrangement in $LiMn_{1-x}Fe_xPO_4$ (LMFP). Superexchange interactions were observed to affect the TM structure sequence and magnetic structure in LMFP, indicating that Mn ions tend to have a specific clustering arrangement in the TM layer that is bridged by shared O ions. The overall magnetic structure is antiferromagnetic.

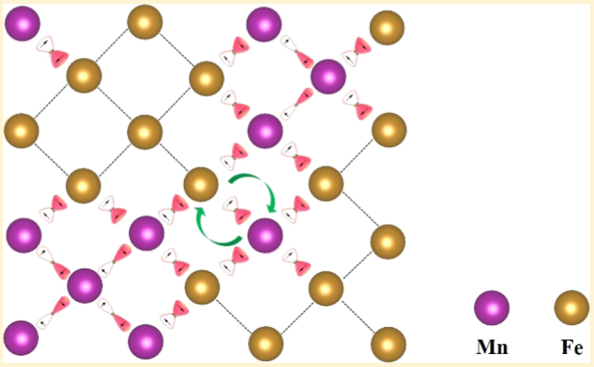

INTRODUCTION

Utilizing lithium-ion batteries (LIBs) is regarded as one of the most efficient means to overcome the lack of liquid fuels and reduce the pollution of urban air. The performance of LIBs is mainly determined by the physical and chemical properties of the cathode material.[1] Olivine-type $LiFePO_4$ has attracted much attention in recent years as a cathode material in LIBs due to its structural stability, high capacity, low cost, and nontoxicity.[2] However, it has a voltage plateau at approximately 3.45 V, which leads to a relatively low power density. With a high voltage plateau (4.1 V vs Li/Li^+) and the same theoretical capacity of 170 mAh/g,[3−5] $LiMnPO_4$ (LMP) has a power density approximately 20% higher than that of LFP, but LMP is often reported to suffer from poor kinetics upon charge/discharge cycling due to Jahn−Teller-active Mn^{3+} ions. Recently,[6,7] the introduction of Mn ions to $LiMn_{1-x}Fe_xPO_4$ (LMFP) materials to increase the voltage and energy storage has become a hot topic in the studies on LFP-type cathode materials.[4]

Yamada et al.[8,9] analyzed the phase diagrams to further explain the influence of Mn on the reversible Li-ion extraction process in $LiFe_{0.4}Mn_{0.6}PO_4$. First, the ions of Fe^{2+} are oxidized to Fe^{3+} at 3.5 V, and then Mn^{2+} is oxidized to Mn^{3+} at 4.0 V during the charging process. Thus, two redox active centers are present in LMFP during the insertion of Li^+ ions. The two different voltage plateaus (3.5 and 4.1 V) for the two redox centers are found in all cases, and the incorporation of Mn^{2+} in the lattice of LFP materials and a wide range of LMFP compositions have been tested by many groups.[10−17] The presence of Mn^{2+} in these cases improves the properties of pure LFP, especially the energy density (by approximately 20%). Previous experimental work has observed two redox peaks during the charging and discharging process of LMFP (these peaks represent two redox reactions, i.e., Fe^{2+}/Fe^{3+} and Mn^{2+}/Mn^{3+}), which indicates the nonuniform arrangement of Fe^{2+}/Mn^{2+} ions at the atomic level.[18−26] However, Paolella et al.[27] found only one wide redox peak in the charging and discharging process of a synthesized LMFP material due to the uniform arrangement of Fe^{2+}/Mn^{2+} ions at the atomic level. The presence of two peaks for LMFP indicates that aggregated regions of Fe and Mn exist in the atomic scale arrangement of the transition-metal (TM) layer. In terms of macrodistribution, Mn and Fe are evenly distributed in the TM layer,[28−35] but the study of the arrangement of Mn and Fe on the atomic scale is limited by experimental means; they only observed a structure similar to the magnetic domain structures in small regions on the subatomic scale, showing that Mn ions may be gathered in a special way. So far, there is no answer to this question.

In our work, we studied the Mn and Fe structure sequence in the TM layer on the atomic scale by ab initio calculations using two methods, i.e., the recursive method and comparing special constructions method. Through the above methods, we found that the most stable LMFP structure is Fe/Mn = 1:1 (x = 0.5). The results show that a special aggregated structure should be more stable than a uniform structure. Additionally, we studied the projected electron density of state (PDOS) and the charge density distribution of the most stable structure. The results indicate three kinds of superexchange interactions (Mn−O−Mn, Mn−O−Fe, and Fe−O−Fe) with different intensities in LMFP materials. By studying the local structure energy, we determined that the three superexchange interactions can affect the TM ion arrangement in the TM

Received: April 29, 2019
Revised: June 15, 2019
Published: June 19, 2019

DOI: 10.1021/acs.jpcc.9b04003
J. Phys. Chem. C 2019, 123, 17002−17009

layer and the magnetic structure of LMFP. The results also show that Mn ions tend to have a specific clustering arrangement in the TM layer and are bridged by shared O ions, and the magnetic structure is antiferromagnetic in the most stable configuration. Therefore, our study provides an important reference for research on two- or multielement material structures and the design of LMFP materials.

COMPUTATIONAL METHODS AND MODEL SYSTEMS

The atomic and electronic structures of TM oxides are computed within the framework of spin-polarized density functional theory (DFT) by the Vienna ab initio simulation package.[19−21,36] The exchange−correlation generalized gradient approximation[22,37] and the Perdew−Burke−Ernzerhof method[23,24,38,39] are applied to describe the interactions between valence electrons and core ions. All of the atomic positions and cell parameters are fully relaxed until the force on each atom is less than 0.001 eV/Å and the energies converge to within 1×10^{-5} eV per atom. Brillouin-zone integrations are approximated by using *k*-points of a $4 \times 3 \times 4$ grid. Due to the strongly correlated d bands in the transition metal Mn, the PBE + *U* approach with $U = 3.9$ eV for Mn and $U = 5.3$ eV for Fe, as suggested by previous DFT calculations[14,40] is applied in all calculations. The wave functions are expanded in plane waves up to a kinetic energy cutoff of 520 eV.

RESULTS AND DISCUSSION

Crystal Structures. Figure 1 presents the crystal structure of olivine-type LFP. The relaxed lattice parameters in the orthonormal space group *Pnma* are $a = 10.3377$ Å, $b = 6.0112$ Å, and $c = 4.6950$ Å.[41] For the $1 \times 2 \times 2$ supercells that we selected for the calculation, $a = 10.447$ Å, $b = 12.170$ Å, and $c = 9.507$ Å, respectively, which are consistent with the experimental values. All of the Fe sites are the same. The initial structure of the LMFP crystal is constructed by substituting Fe ions with Mn ions. All Fe and Mn ions are coordinated with six O ions to form FeO_6 and MnO_6 octahedrons in LMFP.[9] Previous work established that Fe^{2+} and Mn^{2+} ions in LMFP are in a high-spin state.[10] Subsequently, these octahedral form a two-dimensional network attached to the (100) plane by shared O ions. After the use of a recursive method to find the most stable structure in the first part, half of the Fe atoms are replaced by Mn atoms, and various sequences of Mn ions in the TM layer are chosen to build the calculation structures. Each structure contains two TM layers.

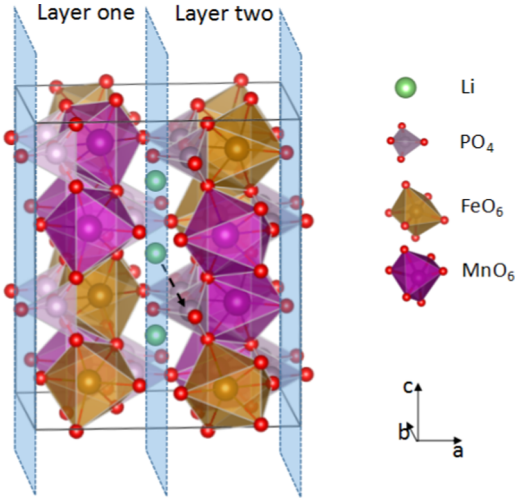

Figure 1. Structure of $LiMn_xFe_{1-x}PO_4$. The plane shown in the figure is a lithium-ion plane, and we use two TM layers, as shown in the figure and marked as layer 1 and layer 2. The yellow, purple, silver, green, and red spheres represent Fe, Mn, P, Li, and O, respectively.

Finding the Lowest-Energy Structure and Magnetic Structure by Using a Recursive Method. First-principles calculation is utilized to calculate the energy of different structures. It is believed that a structure with lower energy will be more stable. The lowest-energy structure detected using recursive search process is shown in Figure 2a. To find the most stable structure of the material, the pure LFP structure is applied as the initial structure, and then the Fe ions are replaced one by one with Mn ions. The energy of replacing Fe^{2+} with Mn^{2+} at different positions is calculated. The position with the lowest energy is found, and the structure with this doping position is recorded as the most stable structure when replacing a Fe atom. In the same way, after the most stable structure is found in the previous step, the most stable structure of the higher-Mn-doped LMFP can be determined by comparing the energies among various structures after the substitution of another Fe ion. Similarly, after the most stable structure of LMFP in which *N* Fe ions are replaced has been found, the next Fe ion is replaced with a Mn ion, and the energies of different substitution structures are calculated. The lowest-energy structure is found to be the most stable structure of LMFP when $N + 1$ Fe ions are replaced. By this method, we find the most stable structures in different situations with different contents of Mn ions. We can infer that when the ratio of Fe and Mn ions is 1:1, the most stable structure is formed, as shown in Figure 2b. From the results, we find that the Mn ions in the TM layer have a tendency to aggregate to form a structure sequence by sharing O ions.

Comparing Special Structures to Determine the Most Stable Structure. A large number of different structure sequences in $1 \times 2 \times 2$ supercells are constructed, and eight structural representations (Figure 3I) are selected. We adopt three representative magnetic structures, as shown in Figure 3II. We compare the calculated energies of the different structure sequences for each magnetic structure. According to Figure 3II, the first is the TM ion (Fe, Mn) ferromagnetic structure; the second is the Fe−Fe and Mn−Mn ferromagnetic structure in which all Mn ions have a magnetic moment against all Fe ions; and the third is the TM ion (Fe, Mn) antiferromagnetic structure.

The calculated energy results are shown in Table 1. (1) Considering the difference between the vertical and horizontal energy, the effect of the magnetic structure on the energy is greater than that of the TM ion sequence. (2) The antiferromagnetic structure (the third magnetic structure shown in Figure 3II) presents a lower energy than the other magnetic structures, indicating that it is more stable. (3) In regards to the effect of the sequence of Mn−Fe ions on the energy, it could be observed that the aggregated structures ((a), (b)) are more stable than the uniform structure (g). From (a) to (h), the structures shown in Figure 3I are aggregated ((a),(b)), random ((d), (e)), two-phase (c), nearly uniform (f), uniform (g), and opposite (h); and the energy is displayed in this order from low to high. Therefore, Mn ions in

DOI: 10.1021/acs.jpcc.9b04003
J. Phys. Chem. C 2019, 123, 17002−17009

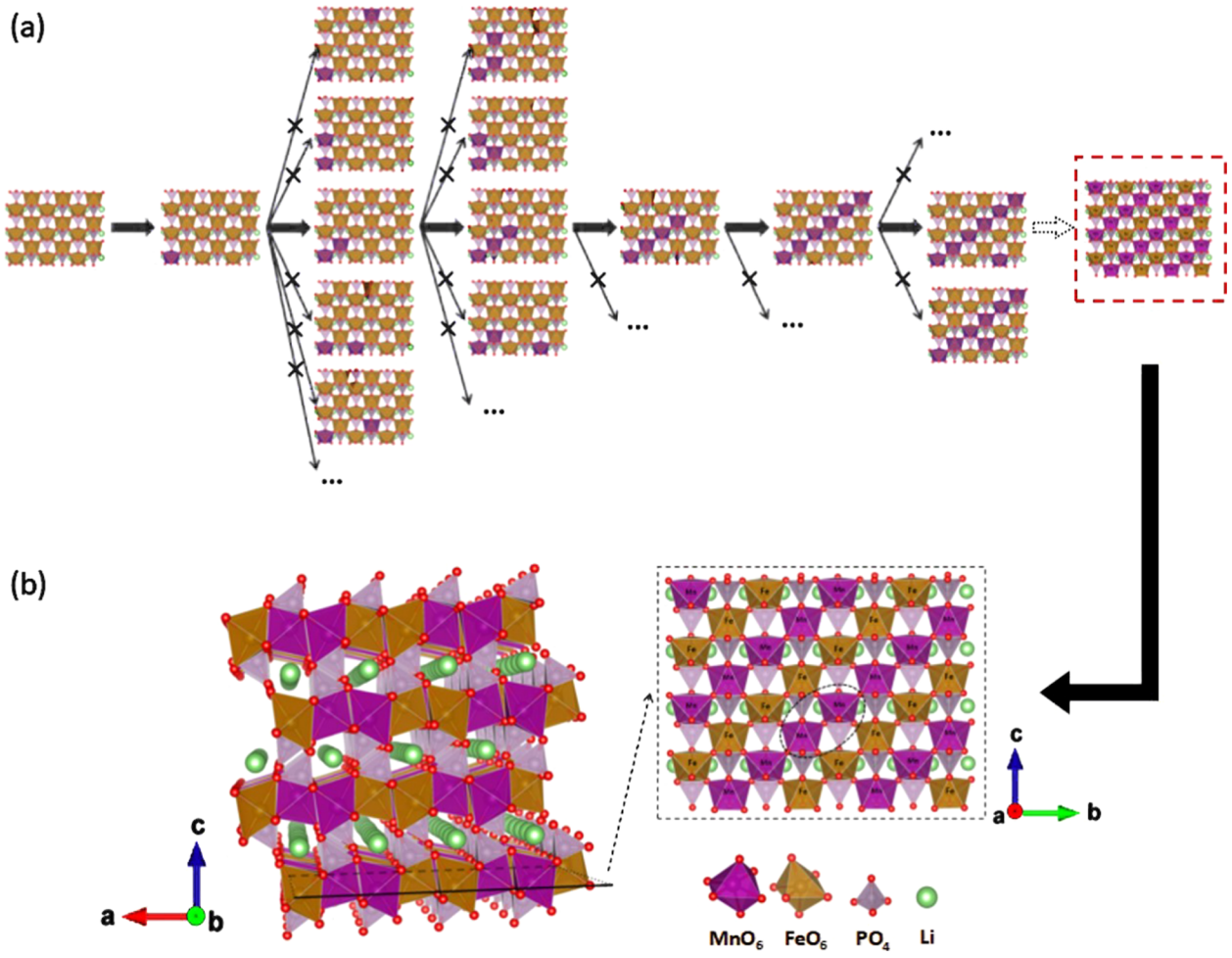

Figure 2. (a) Results of using the recursive method to find the most stable structure with different concentrations of Mn ions. (b) The most stable structure was under the condition of Fe/Mn = 1:1 (x = 0.5 in $LiMn_{1-x}Fe_xPO_4$).

the TM layer tend to have a specific sequence, and Mn ions are more likely to be bridged by sharing O ions.

SUPEREXCHANGE INTERACTION: THE ORIGIN OF THE ANTIFERROMAGNETIC STRUCTURE IN LMFP

The magnetic moment and sequence results are derived from the superexchange interaction. The superexchange interaction has been found in MnO in previous work.[42] In the TM layer of LMFP, the Mn ion is present as Mn^{2+} under full lithiation conditions. Similar to the situation in MnO, the superexchange interaction might exist here, which transforms the magnetic structure into an antiferromagnetic structure and causes the Mn ions in the TM layer to aggregate into a structure sequence. In the TM layer, the large distance between TM ions results in a weak direct-exchange interaction. The electron structure of the O^{2-} ion is $(1s)^2\ (2s)^2\ (2p)^4$, and the electron cloud in the O 2p orbital can overlap with the electron cloud in the Mn 3d orbital. One electron in the O 2p orbital can transfer to the Mn 3d orbital. According to Hund's Rule, the magnetic moment of this electron can only be antiparallel to that of the five electrons of Mn^{2+} in the Mn 3d orbital. In the meantime, the spins of the two electrons in the O 2p orbital must be antiparallel. Moreover, the same interaction between the second electron in the O 2p orbital and another Mn^{2+} transforms the magnetic moment of the two Mn^{2+} linked to the same O ion in the opposite direction. Finally, the antiferromagnetic structure is formed.

Analysis of the Projected Electron Density of States. The overall electron DOS of the LMFP is calculated (as shown in Figure 4a). In the position of $E - E_f = -1$ eV, the projected density of states (PDOS) of Mn shows a peak, as well as the state density of O. However, the PDOS of the O^{2-} ion does not present a peak in the same position in LFP (Figure S1), indicating that the outermost electron in the 3d orbital of the Mn ion can overlap with the outermost electron in the O 2p orbital. It is a necessary condition for the existence of the superexchange interaction.

To further prove the superexchange interaction in LMFP materials, O ions in different positions are selected to calculate the PDOS. As shown in Figure 4, in the supercell with the lowest-energy and magnetic structures, the local structure, which contains O ions in all different positions, is taken out (Figure 4b). There are three types of O ions in the TM layer of LMFP, which are $O_{(1)}$ $O_{(2)}$, and $O_{(3)}$. As Figure 4c reveals, five PDOS, i.e., Mn 3d orbital linked with O, Fe 3d orbital linked with O, 2p orbital of $O_{(1)}$, 2p orbital of $O_{(2)}$, and 2p orbital of $O_{(3)}$, are calculated. After comparison, it is observed that at the position of −1 eV, the PDOS of the Mn^{2+} ion shows a peak, indicating the local position of the outermost electron in the 3d orbital. $O_{(1)}$ is the O ion shared by two Mn ions (Mn−$O_{(1)}$−Mn), which is represented by the obvious peak at −1 eV,

DOI: 10.1021/acs.jpcc.9b04003
J. Phys. Chem. C 2019, 123, 17002−17009

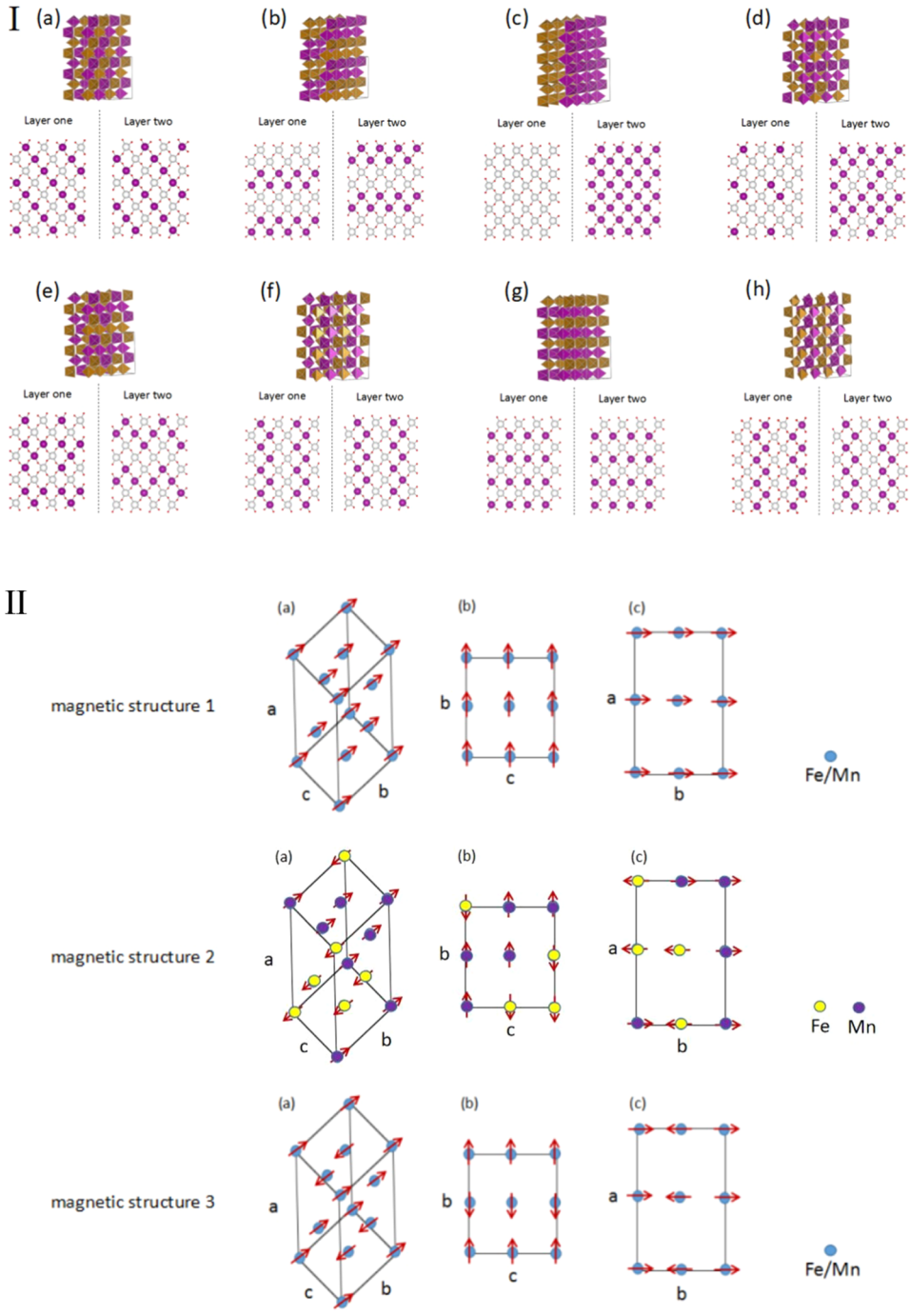

Figure 3. (I) Eight representative ordered structures shown in (a)−(h) (when $x = 0.5$ in $LiMn_{1-x}Fe_xPO_4$). In each figure, the upper graph is the structure, and the two lower figures show different Mn atoms in two TM layers. The positions of the Mn atoms in the TM layer are marked with purple spheres. (II) The three representative magnetic structures are shown. Magnetic structure 1 is a ferromagnetic structure; in magnetic structure 2, the spin direction of the iron atoms is opposite to that of the manganese atoms; and magnetic structure 3 is the antiferromagnetic structure. In the magnetic structures 1 and 3, the spin directions of each atom are related to its position. In each magnetic structure, panel (a) shows the magnetic moment of each TM ions in the structure, panel (b) is the projections onto the *bc* plane [top view of panel (a)], and panel (c) is the projections onto the *ab* plane [right view of panel (a)].

which is the same as that of the Mn ion. $O_{(2)}$ is the O ion shared by an Mn ion and a Fe ion (Mn−$O_{(2)}$−Fe), which is also represented by the peak at the same position but is lower than the peak of $O_{(1)}$. $O_{(3)}$ shared by two Fe ions (Fe−$O_{(3)}$−Fe) does not show a special peak in the PDOS. Hence, the outermost electrons in the O 2p orbital are not affected or limited by the Fe ions.

To measure the influence of $O_{(1)}$, $O_{(2)}$, and $O_{(3)}$ ions on superexchange, the integral DOS of the O 2p orbitals for the above three types are calculated for the integral interval from $E_1 = -1.56$ to $E_2 = -0.56$ (the range in blue is shown in Figure 4c). The integral state density results are as follows: the integral value of $O_{(1)}$ in the region is 0.205; the integral value of $O_{(2)}$ in the region is 0.131; and the integral value of $O_{(3)}$ is

DOI: 10.1021/acs.jpcc.9b04003
J. Phys. Chem. C 2019, 123, 17002−17009

Table 1. Three Magnetic Structures and the Energy Calculation of the Different Structures (from (a) to (h)): Two-Phase, Random, Nearly Uniform, Uniform, and Opposite[a]

	regularly gathered		two-phase	random		nearly uniform	uniform	opposite
	a (meV)	b	c	d	e	f	g	h
magnetic structure 1	167	171	181	179	187	202	216	243
magnetic structure 2	63	68	147	96	71	108	38	157
magnetic structure 3	0	3	17	11	12	29	38	64

[a]Minimum energy has been subtracted from all results (the energy of structure a under the conditions of magnetic structure 3) to make the difference obvious.

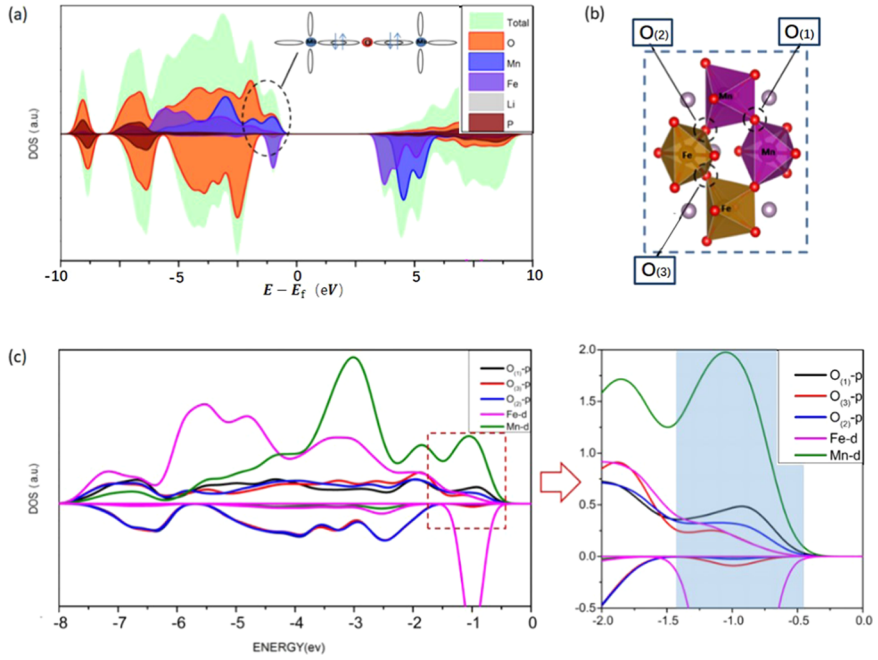

Figure 4. (a) Electronic density of states (DOS) of $LiMn_{(1-x)}Fe_xPO_4$ ($x = 0.5$; under the conditions of structure a). In the position of $E - E_f = -1$, the state density of Mn shows a peak as well as the state density of O. (b) The three types of oxygen ions in the TM layer of LMFP. (c) The PDOS of target ions (top−down ions): 3d orbital in Mn^{2+}, 3d orbital in Fe^{2+}, p orbital in $O_{(1)}$ (the oxygen ion shared by two Mn ions), p orbital in $O_{(2)}$ (the oxygen ion shared by a Mn ion and a Fe ion), p orbital in $O_{(3)}$ (the oxygen ion shared by two Fe ions).

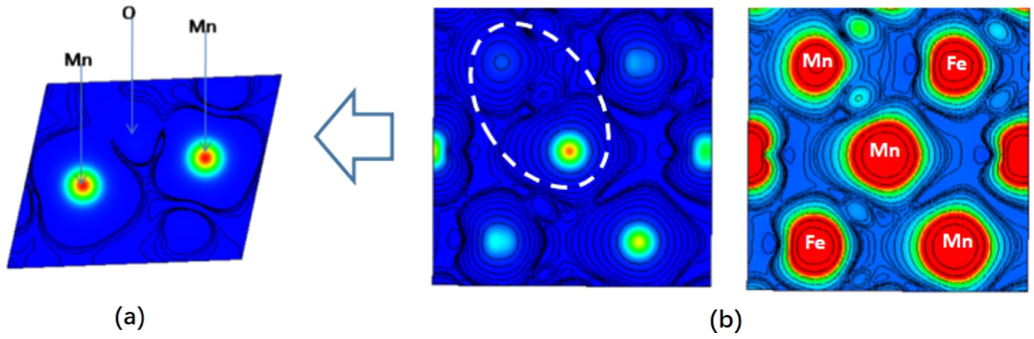

Figure 5. Charge density distribution of the structure in Figure 3I,a (the lowest-energy structure). (a) The local charge density distribution of Mn−O−Mn, which is circled from (b). (b) The charge density distribution of the TM layer of LMFP.

0.077. The integral value of the Mn ion in this region is 0.874 (Figure S2).

According to the analysis of the overall DOS, PDOS, and integral state density, some conclusions can be drawn. In the TM layer, Mn ions can influence the surrounding O ions. The electron cloud in the O 2p orbital can overlap with the electron cloud in the Mn 3d orbital. The outermost electron of the O ion transfers to the Mn 3d orbital. Meanwhile, the O ions shared by two Mn ions are greatly affected, while Fe ions have less impact on the O ions linked to them. There are three kinds of superexchange interactions, i.e., Mn−$O_{(1)}$−Mn, Mn−$O_{(2)}$−Fe, and Fe−$O_{(3)}$−Fe, and the Mn−O−Mn superexchange interaction is stronger than the others.

Figure 5 shows the charge density distribution calculated by adopting the structure of Figure 3I,a (the lowest-energy structure). From the charge density distribution in Figure 5, it can be seen that the outermost electron clouds of the Mn and

DOI: 10.1021/acs.jpcc.9b04003
J. Phys. Chem. C 2019, 123, 17002−17009

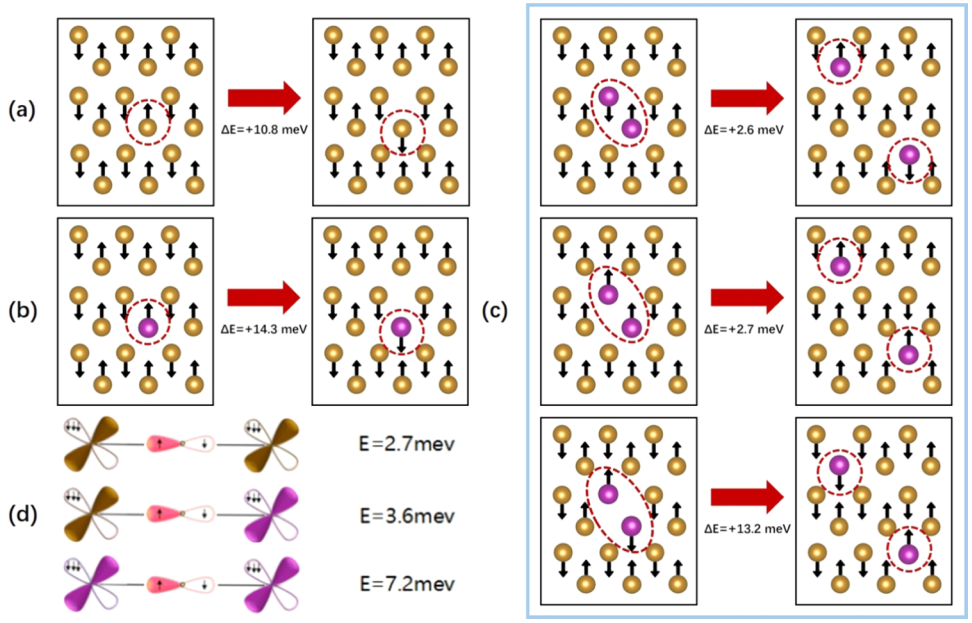

Figure 6. (a, b) Energy change caused by the change in the atomic spin direction. The target atom is Fe in (a), and the target atom is Mn in (b). (c) The energy change caused by the two Mn ions in the distribution were clustered and separated in three different spin cases (according to the direction of the magnetic moment of Mn ions, there are three cases: (1) the magnetic moment of one of the two Mn ions is in the same direction as the magnetic moment of the Fe ion in the substitution position and the other has the opposite magnetic moment. (2) Both Mn ions are in the same direction as the magnetic moment of the Fe ion in the substitution position. (3) Both Mn ions are opposite the direction of magnetic moment of the Fe ion in the substitution position). (d) The energy influence of the three different superexchange interactions: Fe−O−Fe, Fe−O−Mn, and Mn−O−Mn.

O ions overlap, which confirms the existence of superexchange interactions in LMFP materials.

Further Calculation of the Superexchange Energy. To further study the influence of the superexchange interaction on the material structure in LMFP, we choose a suitable stable structure with two TM layers, including 36 transition-metal ions. The antiferromagnetic structure is chosen as the initial magnetic structure of the system. As shown in Figure 6, by selecting the target atom and changing its magnetic moment, the change in the system energy is calculated as shown in the right (2−1, final system is 2, previous system is 1). To judge the degree of influence of the superexchange interaction in different cases, we perform a study as shown in Figure 6a−c. In this study, we only change the magnetic moment direction of the target atom to ensure that the other conditions are the same as before. The supercell is large enough to ensure that the magnetic moment changes of the target ions have little influence on the environment of the ions when the supercell experiences periodic expansion in the calculation, so the energy change in the system is only caused by the change in the magnetic moment of the target ion.

There are three superexchange interactions in the local area of LMFP: (1) the superexchange interaction of an Fe ion with another adjacent Fe ion through an O ion. (2) The superexchange interaction of a Mn ion with an adjacent Fe ion through an O ion. (3) The superexchange interaction of a Mn ion with an adjacent Mn ion through an O ion. To explore the superexchange interaction between the Fe ion with an adjacent Fe ion in the first case, as shown in Figure 6a, the pure LFP structure is selected as the initial structure. The target ion is set to be a Fe ion. By changing the direction of the magnetic moment of the target Fe ion, the energy of the new system is improved with an energy difference of E = 10.8 meV. To explore the superexchange interaction between the Mn ion with an Fe ion in the second case, the initial structure is designed as shown in Figure 6b, in which the target Fe ion in the pure LFP structure is replaced by an Mn ion. After changing the direction of the magnetic moment of the target Mn ion, the increased energy of the system is E = 14.3 meV.

We perform the following calculations to determine how the superexchange interaction causes the Mn ions in the TM layer to aggregate. As shown in Figure 6c, two Fe ions are substituted with Mn ions. The Mn ions in the left structure are clustered, while those in the right structure have a separated distribution. The difference in energy for the two situations (separated and clustered) is calculated under the magnetic moments of the two target TM ions.

The calculated results show that (1) in all cases, the energy of the two Mn ions is higher when they are apart than when they are aggregated. This result reveals that Mn ions tend to aggregate and form some structure sequences. (2) As shown in Figure 6c, when both Mn ions are in the same direction as the magnetic moment of the Fe ions in the substitution position, which means that the overall magnetic moment structure of the material is antiferromagnetic, the calculated difference energy will increase by E = 2.6 meV, which is much smaller than that due to the magnetic moment effect on the energy (as shown in Figure 6a, E = 10.8 meV; Figure 6b, E = 14.3 meV). These results can explain the results in Table 1. The change in energy caused by the magnetic structure of the material is larger than that caused by the TM sequence change; the material has an antiferromagnetic structure, and the ordering of the Mn ions presents some randomness. (3) As shown in Figure 6c, the two Mn ions change from aggregation to separation. The actual interaction is the addition of two Mn−O−Fe superexchange interactions and the loss of one Mn−O−Mn superexchange interaction and one Fe−O−Fe superexchange interaction. Figure 6c shows that the value of the

DOI: 10.1021/acs.jpcc.9b04003
J. Phys. Chem. C 2019, 123, 17002−17009

energy difference for aggregation and separation is $E_{(Mn-O-Mn)} + E_{(Fe-O-Fe)} - 2E_{(Mn-O-Fe)} = 2.6$ meV. This difference suggests that the superexchange interaction tends to aggregate Mn ions; different Mn ion structure sequences have varying amounts of three superexchange interactions. For separation, the overall effect of the superexchange interaction on the system is stronger than that for aggregation. In other words, the results of the magnetic moment and sequence are derived from the superexchange interaction. According to previous results, the strength order of the three superexchange interactions is $E_{(Mn-O-Mn)} > E_{(Mn-O-Fe)} > E_{(Fe-O-Fe)}$. The strengths of the three superexchange interactions are roughly calculated with the results in Figure 6a–c, as shown in Figure 6d. The superexchange interaction of Mn–O–Mn is much stronger than the other two superexchange interactions in LMFP.

CONCLUSIONS

In summary, our paper systematically studied the ordering of transition metals in LMFP materials. In our work, the PDOS analysis at the position of $E - E_f = -1$ showed that the state density of O that shared two Mn ions resulted in a peak, as well as the state density of Mn, and the state density of O in other positions did not appear. From the charge density distribution, the outermost electrons overlap between the O ion and Mn ion. These results proved the existence of the superexchange interaction in LMFP. From the energy study, we found three superexchange interactions, i.e., Mn–O–Mn, Mn–O–Fe, and Fe–O–Fe, with different intensities in the LMFP material, and these interactions regulate the magnetic structure and the transition-metal arrangement of the material. Finally, it was verified that an antiferromagnetic structure with Mn ions in the transition metal layer bridged by shared O ions is more stable than other structures.

Our results also show that Mn ions tend to aggregate near each other, resulting in the formation of a local structure similar to the phase separation structure or a special solid solution structure (Mn rings and Fe rings are distributed homogeneously, as shown in Figure 3I,a). Furthermore, the energy difference (17 meV) between the special solid solution structure and the phase separation structure is very small (as shown in Table 1), indicating the two structure arrangements may exist in synthesized LMFP. This may explain the previously reported experiments that sometimes single redox peak was observed in LMFP during electrochemical tests, and sometimes two redox peaks were observed (the phase-separation structure exhibits two redox peaks during charge and discharge, and the solid solution structure exhibits a single redox peak during charge and discharge).

ASSOCIATED CONTENT

Supporting Information

The Supporting Information is available free of charge on the ACS Publications website at DOI: 10.1021/acs.jpcc.9b04003.

Electronic density of states (DOS) of $LiFePO_4$ and the integral DOS of $O_{(1)}$, $O_{(2)}$, $O_{(3)}$, and Mn ions shown in Figure 4b (PDF)

AUTHOR INFORMATION

Corresponding Authors

*E-mail: zhengjx@pkusz.edu.cn (J.Z.).
*E-mail: panfeng@pkusz.edu.cn (F.P.).

ORCID

Feng Pan: 0000-0002-8216-1339

Notes

The authors declare no competing financial interest.

ACKNOWLEDGMENTS

This work was financially supported by the National Natural Science Foundation of China (No. 51672012), Soft Science Research Project of Guangdong Province (No. 2017B030301013), and Shenzhen Science and Technology Research Grant (JCYJ20160226105838578).

REFERENCES

(1) Armand, M.; Tarascon, J. M. Building Better Batteries. *Nature* **2008**, *451*, 652–657.
(2) Padhi, A. K.; Nanjundaswamy, K. S.; Goodenough, J. B. Phospho-Olivines as Positive-Electrode Materials for Rechargeable Lithium Batteries. *J. Electrochem. Soc.* **1997**, *144*, 1188–1194.
(3) Kang, B.; Ceder, G. Battery Materials for Ultrafast Charging and Discharging. *Nature* **2009**, *458*, 190–193.
(4) Sun, C.; Rajasekhara, S.; Goodenough, J. B.; Zhou, F. Monodisperse Porous $LiFePO_4$ Microspheres for a High Power Li-Ion Battery Cathode. *J. Am. Chem. Soc.* **2011**, *133*, 2132–2135.
(5) Gu, L.; Zhu, C.; Li, H.; Yu, Y.; Li, C.; Tsukimoto, S.; Maier, J.; Ikuhara, Y. Direct Observation of Lithium Staging in Partially Delithiated $LiFePO_4$ at Atomic Resolution. *J. Am. Chem. Soc.* **2011**, *133*, 4661–4663.
(6) Delacourt, C.; Poizot, P.; Morcrette, M.; Tarascon, J. M.; Masquelier, C. One-Step Low-Temperature Route for the Preparation of Electrochemically Active $LiMnPO_4$ Powders. *Chem. Mater.* **2004**, *16*, 93–99.
(7) Rui, X.; Zhao, X. X.; Lu, Z.; Tan, H.; Sim, D.; Huey, H. H.; Rachid, Y.; Tuti, M. L.; Yan, Q. Olivine-Type Nanosheets for Lithium Ion Battery Cathodes. *ACS Nano* **2013**, *7*, 5637–5646.
(8) Yamada, A.; Kudo, Y.; Liu, K. Y. Reaction Mechanism of the Olivine-Type $Li_x(Mn_{0.6}Fe_{0.4})PO_4$ ($0 \le x \le 1$). *J. Electrochem. Soc.* **2001**, *148*, A747–A754.
(9) Yamada, A.; Chung, S. C. Crystal Chemistry of the Olivine-Type $Li(Mn_yFe_{1-y})PO_4$ and $(Mn_yFe_{1-y})PO_4$ as Possible 4V Cathode Materials for Lithium Batteries. *J. Electrochem. Soc.* **2001**, *148*, A960–A967.
(10) Hong, J.; Wang, F.; Wang, X.; Graetz, J. $LiFe_xMn_{1-x}PO_4$: A Cathode for Lithium-Ion Batteries. *J. Power Sources* **2011**, *196*, 3659–3663.
(11) Shin, Y. J.; Kim, J. K.; Cheruvally, G.; Ahn, J. H.; Kim, K. W. $Li(Mn_{0.4}Fe_{0.6})PO_4$ Cathode Active Material: Synthesis and Electrochemical Performance Evaluation. *J. Phys. Chem. Solids* **2008**, *69*, 1253–1256.
(12) Chen, L.; Yuan, Y. Q.; Feng, X.; Li, M. W. Enhanced Electrochemical Properties of $LiFe_{1-x}Mn_xPO_4$/C Composites Synthesized from $FePO_4 \cdot 2H_2O$ Nanocrystallites. *J. Power Sources* **2012**, *214*, 344–350.
(13) Burba, C. M.; Frech, R. Local Structure in the Li-Ion Battery Cathode Material $Li_x(Mn_yFe_{1-y})PO_4$ for $0 < x \le 1$ and y = 0.0, 0.5 and 1.0. *J. Power Sources* **2007**, *172*, 870–876.
(14) Wang, Z. H.; Yuan, L. X.; Zhang, W. X.; Huang, Y. H. $LiFe_{0.8}Mn_{0.2}PO_4$/C Cathode Material with High Energy Density For Lithium-Ion Batteries. *J. Alloys Compd.* **2012**, *532*, 25–30.
(15) Zhong, Y. J.; Li, J. T.; Wu, Z. G.; Guo, X. D.; Zhong, B. H.; Sun, S. G. $LiMn_{0.5}Fe_{0.5}PO_4$ Solid Solution Materials Synthesized by Rheological Phase Reaction and Their Excellent Electrochemical Performances as Cathode of Lithium Ion Battery. *J. Power Sources* **2013**, *234*, 217–222.
(16) Martha, S. K.; Grinblat, J.; Haik, O.; Zinigrad, E.; Drezen, T.; Miners, J. H.; Exnar, I.; Kay, A.; Markovsky, B.; Aurbach, D. $LiMn_{(0.8)}Fe_{(0.2)}PO_{(4)}$: An Advanced Cathode Material for Rechargeable Lithium Batteries. *Angew. Chem., Int. Ed.* **2009**, *48*, 8559–8563.

DOI: 10.1021/acs.jpcc.9b04003
J. Phys. Chem. C 2019, 123, 17002–17009

(17) Sun, Y. K.; Oh, S. M.; Park, H. K.; Scrosati, B. Micrometer-Sized, Nanoporous, High-Volumetric-Capacity $LiMn_{0.85}Fe_{0.15}PO_4$ Cathode Material for Rechargeable Lithium-ion Batteries. *Adv. Mater.* **2011**, *23*, 5050−5054.
(18) Di Lecce, D.; Fasciani, C.; Scrosati, B.; Hassoun, J. A Gel-Polymer Sn-C/$LiMn_{0.5}Fe_{0.5}PO_4$ Battery Using a Fluorine-Free Salt. *ACS Appl. Mater. Interfaces* **2015**, *7*, 21198−21207.
(19) Chi, Z. X.; Zhang, W.; Wang, X. S.; Cheng, F. Q.; Chen, J. T.; Cao, A. M.; Wan, L. J. Accurate Surface Control of Core-Shell Structured $LiMn_{0.5}Fe_{0.5}PO_4$@C for Improved Battery Performance. *J. Mater. Chem. A* **2014**, *2*, 17359−17365.
(20) Xiang, W.; Wu, Z. G.; Wang, E. H.; Chen, M. Z.; Song, Y.; Zhang, J. B.; Zhong, Y. J.; Chou, S. L.; Luo, J. H.; Guo, X. D. Confined Synthesis of Graphene Wrapped $LiMn_{0.5}Fe_{0.5}PO_4$ Composite via Two Step Solution Phase Method as High Performance Cathode for Li-Ion Batteries. *J. Power Sources* **2016**, *329*, 94−103.
(21) Oh, S. M.; Myung, S. T.; Choi, Y. S.; Oh, K. H.; Sun, Y. K. Co-precipitation Synthesis of Micro-Sized Spherical $LiMn_{0.5}Fe_{0.5}PO_4$ Cathode Material for Lithium Batteries. *J. Mater. Chem.* **2011**, *21*, 19368−19374.
(22) Guo, X.; Wang, M.; Huang, X.; Zhao, P.; Liu, X.; Che, R. Direct Evidence of Antisite Defects in $LiFe_{0.5}Mn_{0.5}PO_4$ via Atomic-Level HAADF-EELS. *J. Mater. Chem. A* **2013**, *1*, 8775−8781.
(23) Yan, S. Y.; Wang, C. Y.; Gu, R. M.; Li, M. W. Enhanced Kinetic Behaviors of $LiMn_{0.5}Fe_{0.5}PO_4$/C Cathode Material by Fe Substitution and Carbon Coating. *J. Solid State Electrochem.* **2015**, *19*, 2943−2950.
(24) Wang, K.; Hou, M.; Yuan, S.; Yu, H. C.; Wang, Y. G.; Wang, C. X.; Xia, Y. Y. An Additional Discharge Plateau of Mn^{3+} in $LiFe_{0.5}Mn_{0.5}PO_4$ at High Current Rates. *Electrochem. Commun.* **2015**, *55*, 6−9.
(25) Zong, J.; Peng, Q.; Yu, J.; Liu, X. Novel Precursor of $Mn(PO_3(OH))\cdot 3H_2O$ for Synthesizing $LiMn_{0.5}Fe_{0.5}PO_4$ Cathode Material. *J. Power Sources* **2013**, *228*, 214−219.
(26) Xiang, W.; Zhong, Y. J.; Ji, J. Y.; Tang, Y.; Shen, H.; Guo, X. D.; Zhong, B. H.; Dou, S. X.; Zhang, Z. Y. Hydrothermal Synthesis, Evolution, and Electrochemical Performance of $LiMn_{0.5}Fe_{0.5}PO_4$ Nanostructures. *Phys. Chem. Chem. Phys.* **2015**, *17*, 18629−18637.
(27) Paolella, A.; Bertoni, G.; Dilena, E.; Marras, S.; Ansaldo, A.; Manna, L.; George, C. Redox Centers Evolution in Phospho-Olivine Type ($LiFe_{0.5}Mn_{0.5}$ PO_4) Nanoplatelets with Uniform Cation Distribution. *Nano Lett.* **2014**, *14*, 1477−1483.
(28) Lin, Y.; Zeng, B.; Lin, Y.; Li, X.; Zhao, G.; Zhou, T.; Lai, H.; Huang, Z. Electrochemical Properties of Carbon-Coated $LiFePO_4$ and $LiFe_{0.98}Mn_{0.02}PO_4$ Cathode Materials Synthesized by Solid-State Reaction. *Rare Met.* **2012**, *31*, 145−149.
(29) Li, B. Z.; Wang, Y.; Xue, L.; Li, X. P.; Li, W. S. Acetylene Black-Embedded $LiMn_{0.8}Fe_{0.2}PO_4$/C Composite as Cathode for Lithium Ion Battery. *J. Power Sources* **2013**, *232*, 12−16.
(30) Kim, J. K.; Vijaya, R.; Zhu, L.; Kim, Y. Improving Electrochemical Properties of Porous Iron Substituted Lithium Manganese Phosphate in Additive Addition Electrolyte. *J. Power Sources* **2015**, *275*, 106−110.
(31) Xu, J.; Chen, G.; Li, H. J.; Lv, Z. S. Direct-Hydrothermal Synthesis of $LiFe_{1-x}$ Mn_xPO_4 Cathode Materials. *J. Appl. Electrochem.* **2010**, *40*, 575−580.
(32) Ma, J.; Qin, Q. Z. Electrochemical Performance of Nanocrystalline $LiMPO_4$ Thin-Films Prepared by Electrostatic Spray Deposition. *J. Power Sources* **2005**, *148*, 66−71.
(33) Kim, J. K.; Chauhan, G. S.; Ahn, J. H.; Ahn, H. J. Effect of Synthetic Conditions on the Electrochemical Properties of $LiMn_{0.4}Fe_{0.6}PO_4$/C Synthesized by Sol−Gel Technique. *J. Power Sources* **2009**, *189*, 391−396.
(34) Lee, K. T.; Lee, K. S. Electrochemical Properties of $LiFe_{0.9}Mn_{0.1}PO_4/Fe_2P$ Cathode Material by Mechanical Alloying. *J. Power Sources* **2009**, *189*, 435−439.
(35) Yao, J.; Bewlay, S.; Konstantionv, K.; Drozd, V. A.; Liu, R. S.; Wang, X. L.; Liu, H. K.; Wang, G. X. Characterisation of Olivine-Type $LiMn_xFe_{1-x}PO_4$ Cathode Materials. *J. Alloys Compd.* **2006**, *425*, 362−366.
(36) Kresse, G.; Furthmuller, J. Efficient Iterative Schemes for Ab Initio Total-Energy Calculations Using a Plane-Wave Basis Set. *Phys. Rev. B* **1996**, *54*, No. 11169.
(37) Perdew, J. P.; Burke, K.; Ernzerhof, M. Generalized Gradient Approximation Made Simple. *Phys. Rev. Lett.* **1996**, *77*, 3865−3868.
(38) Anisimov, V. I.; Zaanen, J.; Andersen, O. K. Band Theory and Mott Insulators: Hubbard U Instead of Stoner I. *Phys. Rev. B* **1991**, *44*, 943−954.
(39) Blöchl, P. E. Projector Augmented-Wave Method. *Phys. Rev. B* **1994**, *50*, 17953−17979.
(40) Zhou, F.; Marianetti, C. A.; Cococcioni, M.; Morgan, D.; Ceder, G. Phase Separation in Li_xFePO_4 Induced by Correlation Effects. *Phys. Rev. B* **2004**, *69*, No. 201101.
(41) Rousse, G.; Carvajal, J. R.; Patoux, S.; Masquelier, C. Magnetic Structures of the Triphylite $LiFePO_4$ and of Its Delithiated Form $FePO_4$. *Chem. Mater.* **2003**, *15*, 4082−4090.
(42) Anderson, P. W. Antiferromagnetism. Theory of Superexchange Interaction. *Phys. Rev.* **1950**, *79*, 350−356.

DOI: 10.1021/acs.jpcc.9b04003
J. Phys. Chem. C 2019, 123, 17002−17009